RSC Advances

ROYAL SOCIETY OF CHEMISTRY

PAPER

View Article Online
View Journal | View Issue

Check for updates

Cite this: *RSC Adv.*, 2024, **14**, 3321

Berberine mediated fluorescent gold nanoclusters in biomimetic erythrocyte ghosts as a nanocarrier for enhanced photodynamic treatment†

Wrenit Gem Pearl,[a] Rajakar Selvam,[a] Artashes V. Karmenyan,[a] Elena V. Perevedentseva,[b] Shih-Che Hung,[c] Hsin-Hou Chang,[c] Natalia Shushunova,[d] Ekaterina S. Prikhozhdenko,[d] Daniil Bratashov,[d] Valery V. Tuchin[d] and Chia-Liang Cheng*[a]

Received 5th December 2023
Accepted 11th January 2024

DOI: 10.1039/d3ra08299g

rsc.li/rsc-advances

Photodynamic therapy (PDT) is a well-established cancer treatment method that employs light to generate reactive oxygen species (ROS) causing oxidative damage to cancer cells. Nevertheless, PDT encounters challenges due to its oxygen-dependent nature, which makes it less effective in hypoxic tumor environments. To address this issue, we have developed a novel nanocomposite known as AuNC@BBR@Ghost. This nanocomposite combines the advantageous features of erythrocyte ghost membranes, the photoresponsive properties of gold nanoclusters (AuNC) and the anticancer characteristics of Berberine (BBR) for cancer treatment. Our synthesized AuNC efficiently produce ROS, with a 25% increase in efficiency when exposed to near-infrared (NIR) irradiation. By harnessing the oxygen-carrying capacity of erythrocyte ghost cells, AuNC@BBR@Ghost demonstrates a significant improvement in ROS generation, achieving an 80% efficiency. Furthermore, the AuNC exhibit tunable emission wavelengths due to their excellent fluorescent properties. In normoxic conditions, treatment of A549 lung carcinoma cells with AuNC@BBR@Ghost followed by exposure to 808 nm NIR irradiation results in a notable increase in intracellular ROS levels, accelerating cell death. In hypoxic conditions, when A549 cells were treated with AuNC@BBR@Ghost, the erythrocyte ghost acted as an oxygen supplement due to the residual hemoglobin, alleviating hypoxia and enhancing the nanocomposite's sensitivity to PDT treatment. Thus, the AuNC@BBR@Ghost nanocomposite achieves an improved effect by combining the advantageous properties of its individual components, resulting in enhanced ROS generation and adaptability to hypoxic conditions. This innovative approach successfully overcomes PDT's limitations, making AuNC@BBR@Ghost a promising nanotheranostic agent with significant potential for advanced cancer therapy.

1. Introduction

Nanoparticles have shown great potential in medicine and hold a promising role in nanotheranostics.[1] They are no longer regarded solely as simple drug carriers or vehicles for biomedical applications; instead, they actively mediate biological effects. Advanced theranostic nanomedicine focuses on the applications of noble metal nanoclusters (NC), including gold, silver and copper, as biosensors[2] and for imaging-guided cancer therapy.[3] Metal nanoclusters which have sizes comparable to the Fermi wavelength of electrons (∼2 nm) and consist of a few to hundred atoms, serve as a bridge between individual metal atoms and larger nanoparticles.[4] The physicochemical properties of NCs are significantly different from those of nanoparticles due to their discrete energy levels and molecular-like properties.[4,5]

Metal nanoclusters serve as excellent agents for intracellular localization, demonstrating deeper penetration into tumor spheroids[6] and eliminating the need for dyes in imaging.[2] The use of fluorescent nanoclusters in sensing and bioimaging applications has gained popularity due to their attractive optical properties, such as tunable fluorescent wavelengths, long fluorescence lifetimes (>200 ns) and large Stokes shift (>100 nm).[7,8] Therefore, metal nanoclusters offer numerous advantages over organic fluorophores and quantum dots.[9,10] Among metal nanoclusters, gold nanoclusters (AuNC) exhibit a distinct

---

[a] *Department of Physics, National Dong Hwa University, 97401, Taiwan. E-mail: clcheng@gms.ndhu.edu.tw*

[b] *P. N. Lebedev Physics Institute of Russian Academy of Sciences, Moscow, 119991, Russia*

[c] *Department of Molecular Biology and Human Genetics, Tzu-Chi University, Hualien 97004, Taiwan*

[d] *Saratov State University, Astrakhanskaya Str. 83, Saratov, 410012, Russia*

† Electronic supplementary information (ESI) available. See DOI: https://doi.org/10.1039/d3ra08299g

features, including good photostability, biocompatibility,[8] facile synthesis with flexible size tunability,[11] and convenient surface modification options.[12,13] These unique, stable optical and structural properties of AuNC make them highly applicable in various biomedical fields, including imaging, detection, and therapy.[11,14–16]

In recent years, there has been a growing focus on the use of nanoclusters in photodynamic therapy (PDT) for cancer treatment, particularly in the context of generating reactive oxygen species (ROS).[17,18] ROS are highly reactive oxygen-containing free radicals produced during the metabolic activities of cells. In normal cells, ROS generation is balanced by biochemical antioxidants.[19] However, for cancer treatments, an excess of ROS is generated to induce cell death. The effectiveness of PDT using conventional fluorophores or photosensitizers (PS) depends on several factors. These factors include their chemical purity, which should be minimally toxic in darkness but cytotoxic when exposed to light, intracellular localization, rapid excretion to reduce systemic toxicity, efficiency in generating ROS, and the quality of illumination conditions.[20] Despite the abundance of conventional PS in various colors and reactive forms, they have limitations, such as poor water solubility, low singlet oxygen quantum yield, low selectivity for the tumor site and the need for irradiation with a UV or visible wavelength laser.[20] Studies on the interaction of light with biological tissue have revealed that high-energy laser beams have limited tissue penetration and can cause side effects. Therefore, PDT using UV or visible range excitation has corresponding limitations, especially in treating large or deep-seated tumors.[21] In contrast, NIR light offers enhanced spatial selectivity and results in minimal damage to normal tissues.[21,22] It can be considered as a solution to overcome the limitations of conventional PDT. The spectral range from 700 to 1400 nm is known as the biological window because within this range, biological tissues have a much lower molar extinction coefficient. This makes it suitable for deep tissue treatments without harming neighboring tissues.[23] Consequently, a photodynamic agent capable of generating ROS in cancer environment within this range of excitation enables NIR-triggered PDT.

As PDT strongly relies on the local oxygen content within the tumor environment, its efficacy is significantly hampered by hypoxic microenvironments. Therefore, to enhance the efficiency of PDT in hypoxic tumor environments, the delivery of PS alongside oxygen carriers into tumor tissues becomes crucial. Herein, inspired by the nature of erythrocyte ghosts, which serve as novel drug carriers[24–26] and oxygen supplements due to their residual hemoglobin content,[25,27] we present an approach aimed at alleviating hypoxia in tumors and increasing PDT efficiency. Red Blood Cells (RBC), or erythrocytes, constitute the most abundant cell type in the blood and have garnered substantial attention in the field of drug delivery due to their natural compatibility with the immune system. They serve as ideal carriers capable of circulating in the body for an extended period, typically between 70 and 140 days.[28] RBC can undergo reversible swelling when exposed to a hypotonic solution. During this process, the cellular contents are removed, which includes free hemoglobin released from ruptured RBC, and what remains inside the RBC membranes is referred to as residual hemoglobin. This remnant is termed as erythrocyte ghost. The swelling feature permits the drug/nanomaterials to accumulate within RBC. Subsequently, upon incubation, the cells recover their original shape and impermeability.[29] Furthermore, tissue-specific targeting strategies can be enabled by improving the nanoparticle design and the site of injection.[30]

In this study, we synthesized AuNC using the protocol reported by Duff *et al.*[31] These AuNC were then surface-decorated on the Berberine molecules, a co-agent used to achieve highly efficient cancer treatment. Berberine (BBR) is a bitter-tasting, yellow-colored chemical naturally found in the roots, rhizomes, and stem bark of several medicinal plants. It has a long history of use in Chinese and Ayurvedic medicine[32] and is known for its significant antimicrobial, antioxidant, anti-inflammatory, antidiabetic, and anti-cancer properties.[33,34] Berberine's fluorescent properties make it a potential agent for photodynamic activities.[35] In 1984, Philogène *et al.*[35] were the first to demonstrate the generation of singlet oxygen ($^1O_2$) by BBR. Subsequently, BBR's photodynamic activity in cancerous cells was reported: it generates reactive oxygen species and other radicals in the presence of a light source, leading to mitochondrial dysfunction, DNA damage and the activation of apoptosis for cancer treatment.[36–38] The focus of our present study is on the fabrication of a novel oxygen-evolving nanocomposite, AuNC@BBR@Ghost and the assessment of its potential for PDT under NIR irradiation. We observed that the efficiency of ROS generation by BBR was relatively low when excited at 808 nm. However, when AuNC were introduced as surface decorations, the resulting complex (AuNC@BBR) presented intriguing opportunities for future investigations.

2. Experimental section

2.1 Materials and reagents for synthesis

The following materials and chemicals were purchased and used. Hydrogen tetrachloroaurate trihydrate ($HAuCl_4 \cdot 3H_2O$; 99%, Sigma-Aldrich), Sodium hydroxide (NaOH, Sigma-Aldrich), tetrakis(hydroxymethyl)phosphonium chloride (THPC, Fluka), thiolated polyethylene glycol (PEG-SH, M_W = 5000, Creative PEGWorks), Berberine (2,3-methylenedioxy-9,10-dimethoxyprotoberberine chloride, Sigma-Aldrich), Dimethyl sulfoxide (DMSO, Sigma-Aldrich).

2.2 Gold nanoclusters synthesis and AuNC@BBR complex preparation

Gold nanoclusters, 3 nm in size, were synthesized following the protocol reported by Duff *et al.*[31] with slight modifications from our previous work.[39] Briefly, 50 ml of water was taken in a round bottomed flask and then 1.1 ml of 1% THPC (the reducing agent) and 275 µl of 2 M sodium hydroxide were added. The mixture was stirred at 1000 rpm. After two minutes, 2.1 ml of 1% hydrogen tetrachloroaurate was added, leading to a color change from yellow to orange-brown, indicating the formation of gold nanoclusters. Subsequently, 1 mM PEG-SH was added as a capping agent, followed by 1 h incubation at room temperature. The solution was then filtered through a 0.22 µm nitrocellulose membrane and stored at 4 °C. The estimated AuNC concentration was approximately 6.7×10^8 nanoparticles per ml.

Berberine was initially dissolved in dimethyl sulfoxide (DMSO) to create stock solutions. To achieve the desired concentration of BBR solution, the stock solution was diluted with DD water. The AuNC@BBR complex was formed by combining 0.01 μM of AuNC and 20 μM of BBR in 2 ml of DD water, followed by 2 h of agitation. This resulted in an AuNC-to-BBR concentration ratio of 0.01 : 20 μM. Subsequently, the mixture was centrifuged at 8000 rcf for 20 minutes, the supernatant was discarded, and the pellet was resuspended in DD water for its intended biological applications.

2.3 Methods of the AuNC@BBR characterizations

The UV-visible absorption spectra of AuNC, BBR and AuNC@BBR complex solutions were measured using UV-visible spectrometer (JASCO V-550, Japan). The morphology and size of AuNC and AuNC@BBR complex were visualized using High-resolution Transmission Electron Microscope (HR-TEM, JEOL JEM-F200). Samples for HR-TEM were prepared on copper grids. Samples were prepared by adding a drop of a solution on a grid placed on filter paper and allowing the solvent to evaporate. The hydrodynamic particle size and zeta potential were characterized using the Zetasizer Nano ZS (Malvern Instruments, Malvern, UK) with a 633 nm wavelength He–Ne laser source on the dynamic light scattering method.

2.4 Preparation of erythrocyte ghost membrane and loading of AuNC@BBR

Fresh mice blood was collected from C57BL/6 mice (5 months old) and was transferred into the EDTA-covered anticoagulant tubes to prepare erythrocyte ghosts. The research methods were approved by the Research Ethics and Use Committee of Buddhist Tzu Chi General Hospital (IACUC no. 110081). Erythrocyte ghosts were prepared with modifications from previous reports.[40,41] Initially, whole blood was centrifuged at 1500 rcf for 5 min at room temperature (HERMLE Z 323 K, Germany), and the colorless plasma was discarded. The resultant RBC were washed thrice with a 1 : 3 ratio of 1 × PBS and then collected by centrifugation at 3400 rcf at room temperature for 1 minute. RBC ghosts were obtained by treating the RBC with a hypotonic solution (0.1 × PBS), which led to the release of cellular contents such as free hemoglobin, enzymes, lipids, and electrolytes. This mixture was centrifuged at 20 000 rcf for 40 min at 4 °C to collect the remnant RBC ghosts, removing intracellular components. The resulting RBC ghosts were washed thrice with PBS buffer and stored in PBS at 4 °C.

Loading of AuNC@BBR with erythrocyte ghosts involved mixing 200 μl of AuNC@BBR solution (0.01 : 20 μM concentration) with 500 μl of RBC ghosts. The mixture was thoroughly agitated in an orbital shaking incubator at 4 °C for 24 h.

2.5 Assessing oxygen-carrying capacity of RBC ghosts with AuNC@BBR loading

To investigate the deoxygenation and oxygenation abilities of erythrocyte ghosts, with and without AuNC@BBR, we employed a UV-visible absorption spectrometer. Deoxygenation was achieved by purging with nitrogen gas, using a 5 μl : 1000 μl ratio of ghost suspension in PBS. The oxygenation–deoxygenation process was conducted, and absorption spectra of erythrocyte ghost solutions, with and without AuNC@BBR, were recorded at 3 minute intervals in the 350 to 650 nm wavelength range. Data analysis was performed using Excel's LINEST function, following the methods outlined in the earlier study.[42] The oxygen saturation was calculated using the following formula:

$$\%\ \mathrm{O_2}\ \text{saturation} = \left(\frac{A_{\text{sample}} - A_{\text{deoxy}}}{A_{\text{oxy}} - A_{\text{deoxy}}}\right) \times 100$$

where A_{sample} is the measured absorbance of the ghost sample, A_{deoxy} is the absorbance of the deoxygenated reference, and A_{oxy} is the absorbance of the fully oxygenated reference.

2.6 Cell culture

The A549 human lung carcinoma epithelial cell line (ATCC number: CCL-185) was cultured in a RPMI 1640 medium supplemented with 10% foetal bovine serum (Gibco, Invitrogen, UK). Normoxic cells were incubated at 37 °C in a humidified incubator (310/Thermo, Forma Scientific, Inc., Marietta, OH) with 5% CO_2, while hypoxic cells were incubated in an anaerobic chamber (Don Whitley DG250 Anaerobic workstation, UK) at 37 °C with 95% nitrogen, 5% CO_2 and 0.2% O_2. The culture medium was replaced with fresh medium every 48 or 72 h, and cells were subcultured when reaching approximately 80% confluence.

2.7 Confocal fluorescence microscopic imaging

A549 cells (1×10^4 cells per well) were seeded in Petri dishes with coverslips and incubated at 37 °C for 24 h. Subsequently, the medium was replaced with fresh medium containing AuNC and BBR solutions, followed by a 6 h incubation. Afterward, the cells were washed with PBS and fixed in 4% formaldehyde in PBS. Fluorescence images were captured using a Leica laser-scanning confocal fluorescence microscope (TCS SP5, Mannheim Germany) equipped with 40 × 1.25 oil immersion objective. AuNC and BBR were excited at 514 nm and 405 nm wavelengths, respectively, with signal collection in the spectral range of 610–660 nm for AuNC and 540–565 nm wavelength for BBR.

2.8 Bio-interaction of AuNC@BBR complex with ghost cells

To observe the interaction of the AuNC@BBR complex with ghost cells, we utilized a Leica laser-scanning confocal fluorescence microscope (TCS SP8 X, Mannheim, Germany) equipped with 100 × 1.25 oil immersion objective (Leica, Mannheim, Germany). Fluorescence from AuNC and BBR was excited using 514 and 405 nm wavelength lasers, respectively. Signal was collected in the spectral range of 610–660 nm for AuNC and 540–565 nm for BBR.

2.9 Measuring reactive oxygen species generation

To assess the efficiency of ROS generation by AuNC, BBR, AuNC@BBR and AuNC@BBR@Ghost, we employed 2′-7′-

dichlorofluorescein diacetate (DCFDA) as a probe (CAS number: 4091990, Sigma-Aldrich) under 808 nm excitation. We used Methylene Blue (MB) as a reference for evaluating ROS generation efficiency.[43,44] DCFDA, a fluorogenic dye, detects hydroxyl, peroxyl and other ROS activities. It involves intracellular diffusion of DCFDA, which is deacetylated by intracellular esterases into a non-fluorescent compound. In the presence of ROS, this compound is oxidized into a fluorescent compound, 2′7′-dichlorofluorescein (DCF),[45] observable at a 502 nm wavelength.

Initially, the UV-vis absorption of the sample solution was adjusted to an optical density (OD) of approximately 0.2. Subsequently, 20 μl of 10 mM DCFDA solution was added to 1 ml of the sample solution, followed by NIR irradiation (808 nm, 0.75 W cm^{-2}) for 30 min. Changes in the absorbance intensity of DCF induced by the samples were recorded every 3 minutes. The efficiency of ROS generation by the sample was calculated using the following equation, with modifications from previous reports:[46]

$$\phi_S = \frac{r_S/A_S}{r_{MB}/A_{MB}}\phi_{MB}$$

where ϕ_S and ϕ_{MB} are the efficiency of ROS generated by the sample and MB respectively. Similarly, r_S and r_{MB} denote the absorption rates of DCFDA under NIR irradiation by the sample and MB, while A_S and A_{MB} represent the integrations of optical absorption bands in the wavelength range of 550 to 800 nm.

2.10 Cell viability study

Cell viability of A549 cells (normoxic and hypoxic) treated separately with AuNC and BBR was assessed using the MTT Assay Kit (Thermo Fisher Scientific, Life Technologies Corporation, Oregon). Cells were seeded at 5 × 10^3 cells per well in a 96 well plate and incubated for 24 h under their respective conditions. Various concentrations of AuNC (2–10 nM) and BBR (5–80 μM) were added, and after 24 and 48 hours, MTT assays were performed. Viable cells converted MTT to purple formazan, which was then solubilized with DMSO, and absorbance was measured at 570 nm using a microplate reader.

2.11 Measurement of reactive oxygen species (ROS assay)

Intracellular ROS generation was analyzed using the DCFDA ROS assay kit. Different groups of samples were prepared in both normoxic and hypoxic conditions, including control groups, groups treated with AuNC, BBR, AuNC@BBR and AuNC@BBR@Ghost solutions with and without NIR laser irradiation. After 10 minutes of NIR laser irradiation (808 nm, 0.75 W cm^{-2}), the cells were incubated for 6 hours, followed by DCFDA staining. Subsequently, we conducted live cell confocal fluorescence imaging and measured fluorescence intensity. These experiments were performed in triplicate across three independent assays.

2.12 Intracellular PDT treatment and live/dead assay

Intracellular PDT treatment and live/dead assay were analyzed to evaluate the PDT efficiency. A549 cells in both normoxic and hypoxic conditions were cultured and treated with solutions containing AuNC, BBR, AuNC@BBR and AuNC@BBR@Ghost solutions for 24 h. Subsequently, these samples underwent photodynamic treatment using NIR laser irradiation (808 nm, 0.75 W cm^{-2}) for 10 minutes and were then incubated for an additional 24 h. Following incubation, cell viability was assessed using the MTT assay for samples both with and without NIR irradiation. To visualize photocytotoxicity, cells were stained with the LIVE/DEAD™ Fixable Violet Dead Cell Stain Kit (L34963) and DiOC5(3). Imaging was conducted using a confocal fluorescence microscope equipped with a 40 × 1.25 oil immersion objective. These experiments were performed in triplicate across three independent assays.

3. Results and discussion

3.1 Characterization of AuNC, BBR, and AuNC@BBR

The fabrication process of AuNC@BBR nanocomposite, illustrated in Fig. 1a, involves two key steps: the synthesis of AuNC, and the surface coating of AuNC onto the BBR molecules. In the initial step, AuNC were prepared and capped with PEG-SH. Subsequently, when these AuNC were introduced to the BBR solution, they adorned the surface of BBR aggregate molecules. Fig. 1(b) presents the UV-visible absorption spectra of AuNC, BBR and AuNC@BBR composite. The absorption spectrum of AuNC exhibits a shoulder around 500 nm, which is the vestiges of the plasmon resonance characteristic peak of a bulk colloidal gold.[31] As THPC-based AuNC are exceedingly small, the surface plasmon resonance absorption peak at 520 nm is suppressed. The UV-vis absorption spectra of the BBR solution reveal three characteristic bands: two maxima bands at around 250 and 350 nm wavelengths and one weaker band at approximately 430 nm. The absorption bands in the 250–350 nm range are attributed to the π → π* transition within the Berberine molecule.[47] The UV-vis absorption spectra of AuNC@BBR shows the characteristic absorption peaks of both AuNC and BBR.

In Fig. 1(c), the hydrodynamic particle sizes of AuNC, BBR and AuNC@BBR are displayed. AuNC exhibited an approximate size of 2 ± 1 nm, indicating minimal aggregation and well-dispersed nanoclusters. The hydrodynamic molecular size of BBR was measured at about 103 ± 18 nm, resulting from the self-assembly of diluted BBR in an aqueous solution, forming nano-sized aggregates. This phenomenon is common among organic π-conjugated systems, which involves a system of alternating single and multiple bonds and tend to form molecular aggregates or stacking structures.[48,49] BBR possesses aromatic rings with positive charges and counter anions. When in an aggregated state, the anions are positioned between the positively charged aromatic rings to hinder π–π stacking. The intermolecular distances of BBR arranged in a parallel manner are measured at 3.851 and 4.090 Å, which exceeds the π–π stacking distance (3.5 Å).[49] For AuNC@BBR, the average particle size was observed to be around 113 ± 22 nm. This increase in size is attributed to the adsorption of AuNC onto the surface of BBR. Importantly, these sizes obtained from DLS align with the observed sizes estimated from HR-TEM images. Moreover, the zeta potential of the particles shifted from −10.5 mV (AuNC) and −13.8 mV (BBR) to −27.1 mV (AuNC@BBR), as depicted in

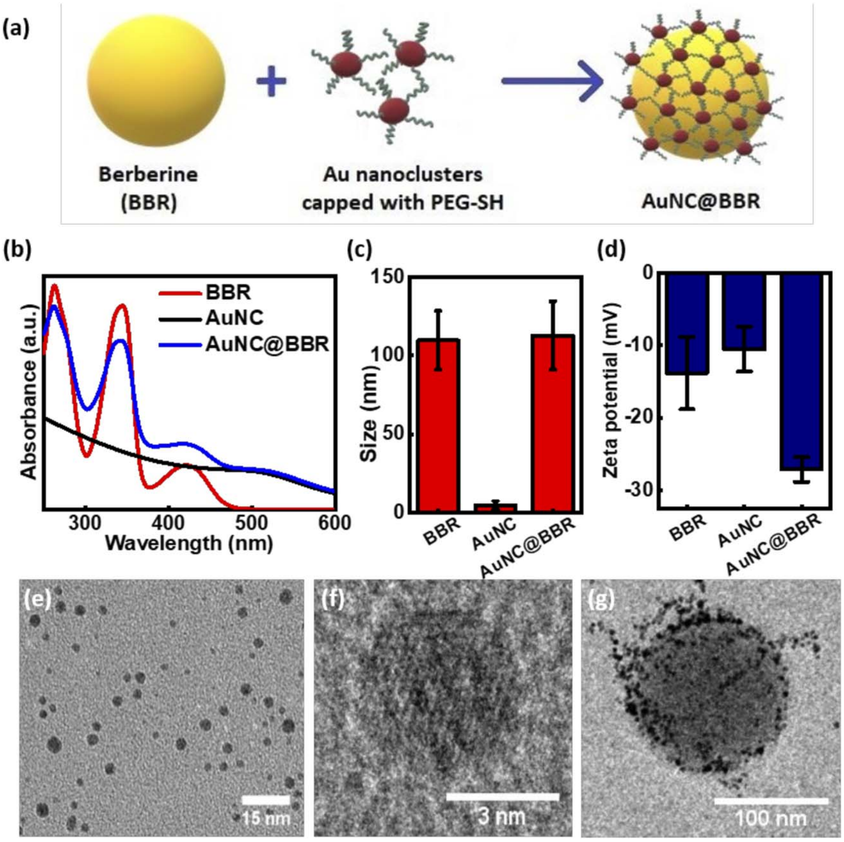

Fig. 1 Synthesis and characterization of AuNC@BBR nanocomposite: (a) schematic depicting the preparation process of AuNC@BBR; (b) UV-visible absorption spectra of AuNC, BBR and the AuNC@BBR composite; (c) hydrodynamic particle sizes and (d) zeta potential of BBR, AuNC and AuNC@BBR in aqueous media; high-resolution transmission electron microscopy (HR-TEM) images of (e) AuNC, (f) a single AuNC, and (g) the AuNC@BBR composite. Scale bar represents 15 nm, 3 nm and 100 nm respectively.

Fig. 1(d). The surface decoration on BBR with AuNC rendered the zeta potential more negative. This increase in negativity signifies that the AuNC@BBR are more stable due to the stronger repulsive forces between them. The HR-TEM image, displayed in Fig. 1(e) and (f), depicts the particle structure of AuNC, indicating an average size of about 1–3 nm, with no signs of aggregation, and well-separated nanoclusters. Upon conjugation of AuNC and BBR, the AuNC are absorbed onto the aggregated BBR, as shown in Fig. 1(g).

Additionally, the average size determined from HR-TEM images was compared with the hydrodynamic particle size measured using the DLS and found to be in good agreement. Using ImageJ software, the coverage of AuNC on the BBR aggregate was quantified from the HR-TEM image, yielding a value of approximately 14.6 ± 3.2%. The quantification process is detailed in Fig. S1 and Table S1.†

3.2 Oxygen-carrying ability of ghosts before and after loading AuNC@BBR

Erythrocyte ghost preparation is depicted in Fig. 2(a). These ghost cells are essentially the remnants of red blood cells stripped of their contents, retaining residual hemoglobin that can serve as a marker for erythrocyte ghost.[25,41] The absorption spectrum in Fig. 2(b) displays key peaks of hemoglobin in oxygenated state: one around 412 nm (Soret band) and bimodal peaks around 540 and 575 nm (Q band) for erythrocyte ghosts. During ghost preparation, each wash step reduces hemoglobin content, leading to decreasing absorption intensity from 100% to 4.8%.

Fig. 2(c) presents hydrodynamic particle sizes: AuNC@BBR at approximately 113 ± 22 nm, ghost at about 829 ± 213 nm, and AuNC@BBR@Ghost at 1099 ± 216 nm. The zeta potential of Ghost is −33.1 mV, indicative of the typical negative charge associated with lipid vesicles.[50] Both intact RBC and ghosts tend to have negative zeta potentials, primarily due to the negative charge associated with the lipid and protein components on their surfaces.[51–53] However, the specific zeta potential of ghost values can vary depending on factors such as the presence of specific lipid components, pH, and ionic strength. For AuNC@BBR@Ghost, the zeta potential is −31.3 mV, suggesting that the AuNC@BBR complex is associated with the ghost.

The deoxygenation and oxygenation ability of hemoglobin in bare ghost and AuNC@BBR@Ghost were examined using UV-vis spectroscopy. In Fig. 2(e) and (f), both bare ghost and AuNC@BBR@Ghost exhibit two absorption peaks located at 428 nm and 565 nm after deoxygenation under nitrogen purging. Three maximum peaks at 412 nm, 540 nm and 575 nm indicate oxygenation.[54–56] Additionally, a time-dependent study of UV-vis

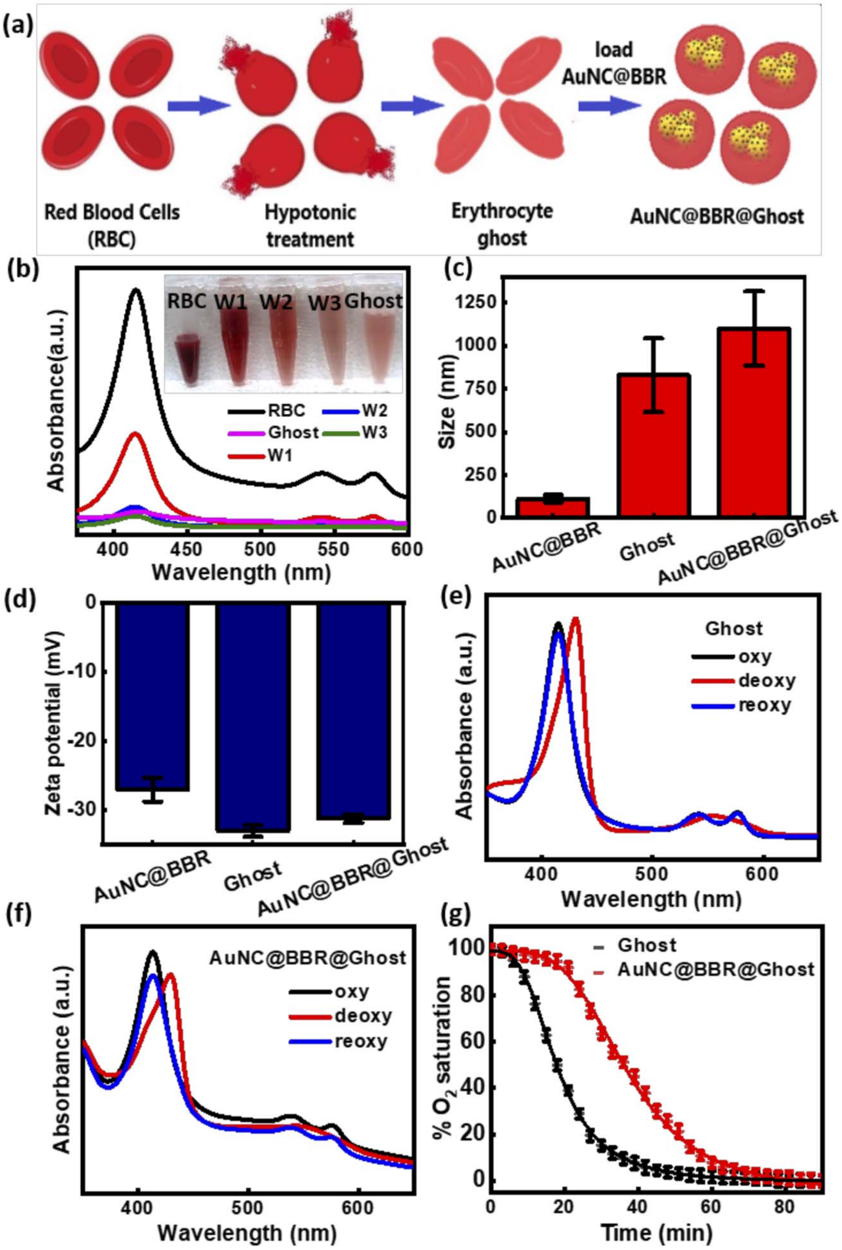

Fig. 2 Characterization of hemoglobin-lysed erythrocyte blood fraction: (a) schematic illustrating the preparation process of ghost and AuNC@BBR-loaded ghost; (b) comparison of UV-vis absorbance spectra at different stages of ghost preparation (inset: color changes during sequential centrifugation and washes); (c) hydrodynamic particle size and (d) zeta potential of AuNC@BBR, ghost and AuNC@BBR@Ghost in aqueous solution; UV-vis absorbance spectra of (e) ghost and (f) AuNC@BBR@Ghost in oxygenated, deoxygenated and reoxygenated conditions; and (g) oxygen-dissociation curves of ghost and AuNC@BBR@Ghost.

absorbance intensity (Fig. 2(g), S3a and b†) shows a similar trend for ghost and AuNC@BBR@Ghost, with AuNC@BBR@Ghost displaying slower reoxygenation. The time difference in half-oxygen saturation time for bare ghost and AuNC@BBR@Ghost are about 20 minutes. This difference likely occurred due to the interaction of AuNC@BBR with the ghosts, which could influence various factors, such as altered binding affinity of hemoglobin for oxygen, diffusion of oxygen in and out of the ghost cells, and the overall oxygenation kinetics. Similar study has been discussed in the ref. 55, 57 and 58 However, the exact mechanisms and factors involved would require further investigation and analysis to understand in detail.

3.3 Fluorescence emission of AuNC and BBR

AuNC exhibit a remarkable and size-dependent fluorescence behavior, a distinctive feature driven by their size-dependent energy levels and electronic transitions. This size-dependent behavior give rise to diverse emission wavelengths in the visible range.[59] To examine the fluorescence properties of the synthesized AuNC, we undertook confocal fluorescence

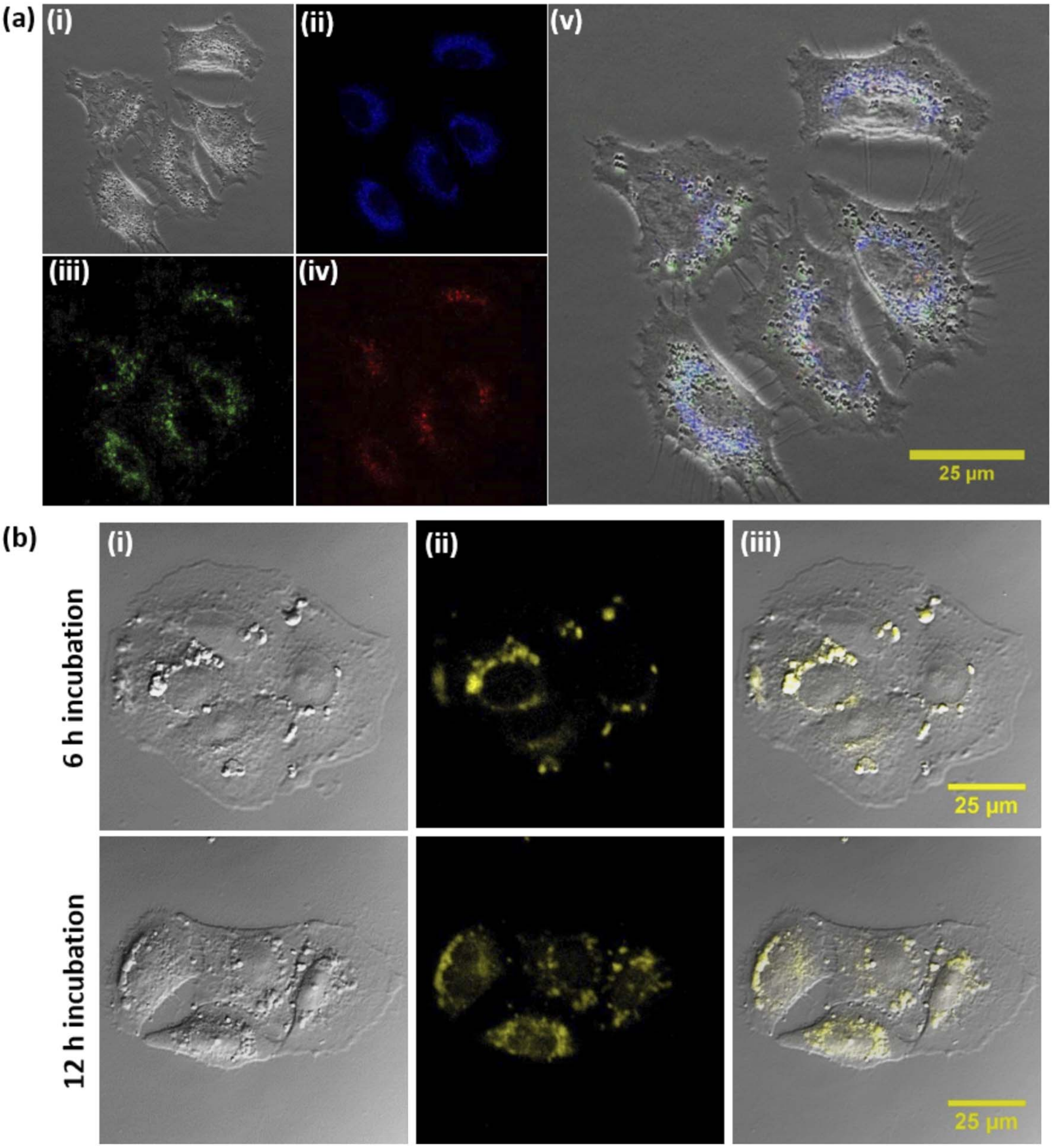

Fig. 3 Fluorescence microscopic images: (a) A549 cells incorporated with AuNCs, emitting RGB fluorescence. With an increasing excitation wavelength, the emission band shifts to longer wavelength, confirming the distribution of nanoclusters sizes. (i) Optical image, (ii) AuNC (ex/em: 405/430–460 nm range, shown in blue), (iii) AuNC (ex/em: 488/510–560 nm range, shown in green), (iv) AuNC (ex/em: 514/610–660 nm range, shown in red) and (v) merged image of (i) to (iv); and (b) fluorescence microscopic images of A549 cells incorporated with BBR (20 μm). (i) Optical image, (ii) BBR (ex/em: 405/540–560 nm) and (iii) merged image of (i) and (ii). Scale bar represents 25 μm. Objective: 40× (oil immersion).

microscopy studies. Fig. 3a illustrates the homogeneous distribution of AuNC within the perinuclear region of A549 cells, emitting fluorescence signals spanning various wavelengths across the visible spectrum, from blue and green to red. As previously noted, both TEM and DLS studies confirmed the average size of these AuNC to be approximately 2–3 nm. Such variations in size could potentially account for the emission tunability, as the energy levels and electronic transitions vary. This tunability makes AuNC promising candidates for applications in areas such as biological imaging, sensing, and optoelectronics.[60]

Berberine is endowed with inherent fluorescent properties, prompting us to employ confocal fluorescence imaging to delve into its cellular uptake. Using a 405 nm wavelength laser, we excited BBR's fluorescence, capturing the emitted signal within the spectral range of 545–560 nm. In Fig. 3b, the image reveals the accumulation of BBR in the perinuclear region of cells after 6 h of incubation. Nevertheless, after a 12 h incubation period, the fluorescence of BBR was observed within the nucleus, with noticeable changes in cellular morphology. This underscores BBR's capacity to induce alterations in the morphology of cancerous cells, further highlighting its potential in anti-cancer applications.[61,62] Therefore, the cellular uptake of AuNC and BBR represents a comprehensive exploration of their fluorescence properties, shedding light on the size-dependent behaviors of AuNC and the distinctive property of BBR.

3.4 Interaction of AuNC@BBR with ghost cells

Given the fluorescence properties of AuNC and BBR, we employed confocal fluorescence imaging to investigate the integration between AuNC@BBR and ghost cells in Fig. 4. Mice blood smear samples were obtained to observe red blood cells under an optical microscope (Fig. 4a). These erythrocytes, measuring approximately 5 μm, exhibited the characteristic biconcave shape. In Fig. 4b, we present the erythrocyte membranes, or ghost cells, obtained from the mice blood. The process of preparing erythrocyte ghosts involves hemolysis of the erythrocytes with a hypotonic medium, which releases cellular contents and free hemoglobin. When these membranes are placed in an isotonic medium, they self-seal, a phenomenon driven by the amphipathic nature of membrane phospholipids.[41] Fluorescence images in Fig. 4c demonstrate the presence of the AuNC@BBR complex within the

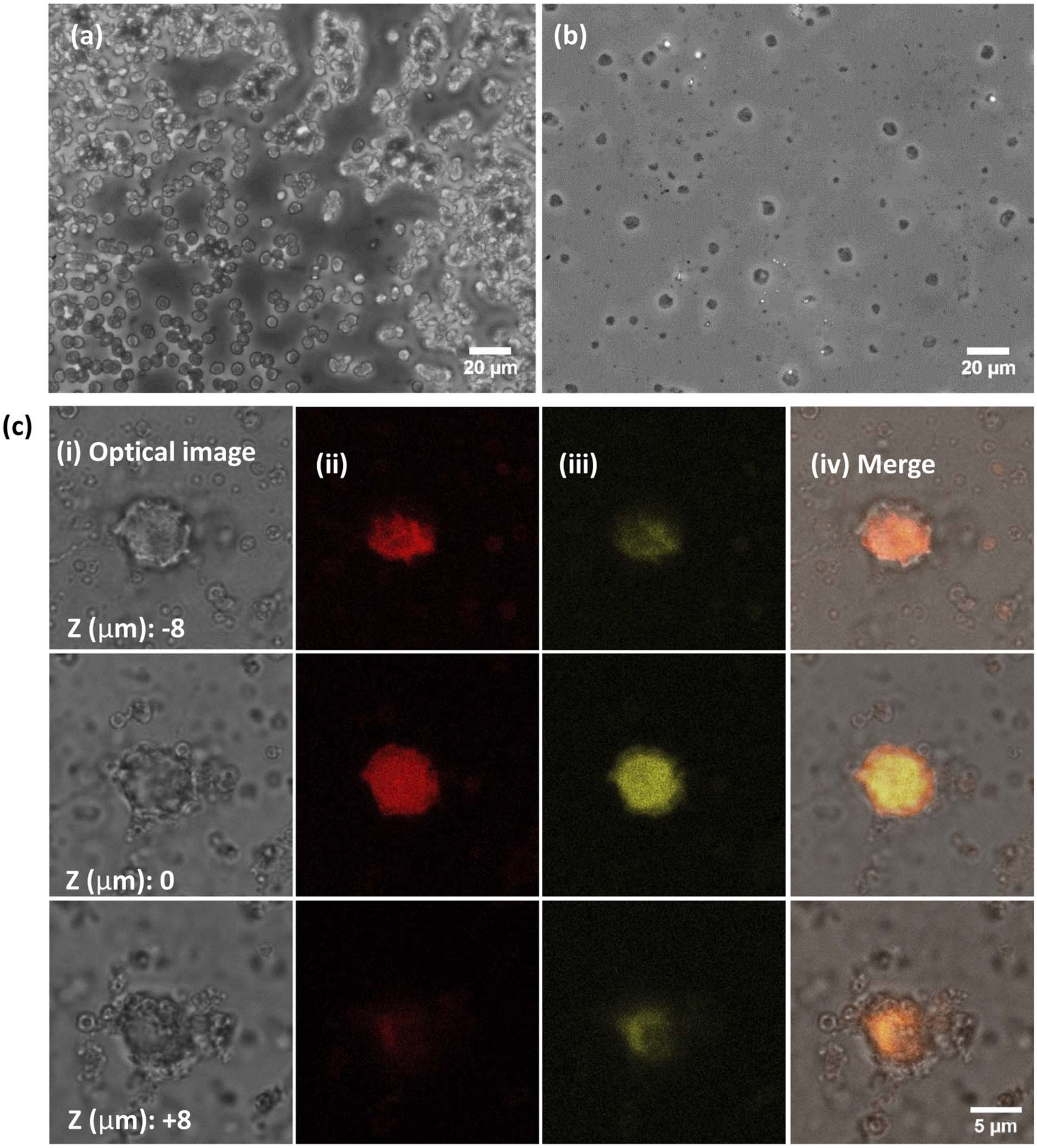

Fig. 4 Structural analysis of RBC, ghost and AuNC@BBR@Ghost: (a and b) optical microscopic images of RBC and ghost respectively. Objective: 40× and the embedded scale bar represents 20 μm; and (c) fluorescence microscopic images of ghost cells incorporated with AuNC@BBR complex at different focal planes. (i) Optical image, (ii) AuNC (ex/em: 514/610–660 nm, shown in red) and (iii) BBR (ex/em: 405/540–560 nm, shown in yellow) (iv) merged image of (i) to (iii). Scale bar represents 5 μm. Objective: 100× (oil immersion).

ghost cells. The z-stacking technique, collecting images at different focal planes, reveals the incorporation of AuNC@BBR complex within the ghost cells. Notably, this incorporation does not affect the structural integrity of the ghost cells, as evidenced by Fig. 4c, 2f and S2,† indicating that the ghost cells maintain their structure, photostability, and oxygen-carrying capacity even after the complex's loading. This observation is crucial for understanding the behavior of AuNC@BBR in biological applications, as it shows that the interaction with ghost cells does not negatively impact their structural and functional properties.

3.5 ROS generation capacity by AuNC@BBR@Ghost nanocomposite under NIR irradiation

The examination of ROS generation was conducted using the commercially available ROS marker DCFDA. Fig. 5 shows the influence of AuNC, BBR and their combination (AuNC@BBR) in the presence or absence of ghost cells (AuNC@BBR@Ghost) on ROS production under NIR irradiation in a PBS buffer solution mixed with DCFDA probe. Fig. 5a illustrates that the control samples, consisting of a PBS buffer solution mixed with DCFDA probe, did not exhibit any increase in DCF absorbance at 502 nm during a 30 minute period of NIR irradiation (808 nm, 0.75 W cm^{-2}). In contrast, when AuNC, BBR, AuNC@BBR and AuNC@BBR@Ghost were mixed with PBS and the DCFDA probe under the same experimental conditions, they all showed an enhancement in DCF absorbance intensity. This suggest that AuNC produces ROS, and AuNC@BBR retains significant ROS generation capabilities. Additionally, the presence of ghost cells led to around a 25% increase in ROS generation by AuNC@BBR@Ghost compared to AuNC@BBR without ghost cells under NIR irradiation. AuNC exhibit unique electrical and optical properties, encompassing size-dependent energy levels, quantum confinement effects, surface plasmon resonance and electron transfer capability. These characteristics collectively enable AuNC to be highly effective in the production of ROS *via* a mechanism known as photo-induced electron transfer (PET).[63] Upon excited by light energy, the electrons in the nanoclusters are excited to higher energy levels and transfer their energy to surrounding oxygen molecules, resulting in the formation of ROS.

To further quantify the ROS generation capacity of AuNC, we performed a time-dependent analysis of the UV-vis absorbance of DCF, induced by AuNC in a PBS buffer solution mixed with DCFDA probe under NIR irradiation, and employed the commercial photosensitizer Methylene Blue (MB) as a reference ($\phi_{MB} \approx 0.5$) to gauge the efficiency of ROS generation. As seen in Fig. 5b–d and S4a,† the DCF absorption increases, indicative of ROS, gradually increased under NIR irradiation for AuNC, AuNC@BBR@Ghost and MB solutions. Their corresponding rate constants are 0.028 min^{-1}, 0.021 min^{-1} and 0.078 min^{-1}, respectively (Fig. 5b inset, 5d and S4b†). We

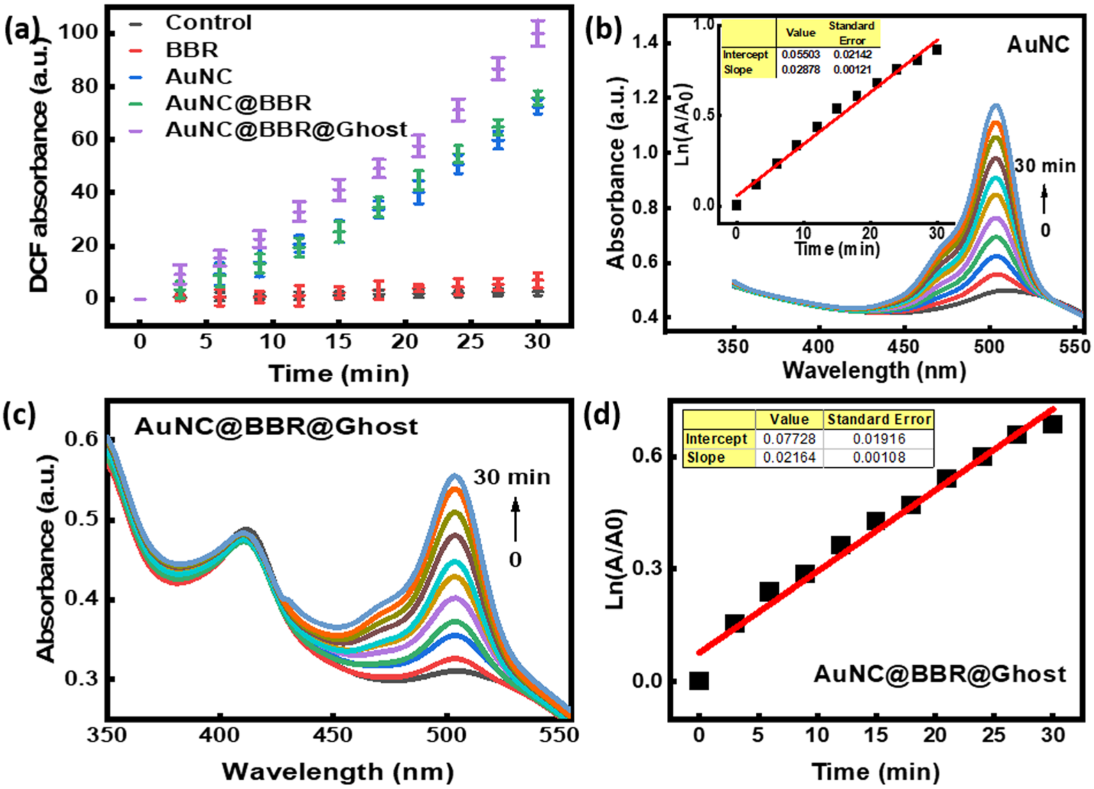

Fig. 5 Time-dependent measurement of ROS generation under NIR irradiation using DCF probe: (a) time-dependent DCF absorbance changes induced by control, BBR, AuNC, AuNC@BBR and AuNC@BBR@Ghost; (b) time-dependent DCF absorbance changes induced by AuNC. The inset shows the rate constants for the AuNC sample under NIR irradiation; (c) time-dependent DCF absorbance changes induced by AuNC@BBR@Ghost; and (d) the rate constants for the AuNC@BBR@Ghost sample under NIR irradiation.

determined that the ROS generation efficiency of AuNC was 25% (see the experimental section and Fig. S4a–d in the ESI† for a detailed explanation of the calculation). Table 1 displays the ROS generation efficiency values obtained for the respective samples. Remarkably, the inclusion of ghost cells increased ROS generation in AuNC@BBR@Ghost, with an ROS generation efficiency of 80%.

3.6 Cytotoxicity study of AuNC and BBR on A549 cells

Fig. 6 presents A549 normoxia and hypoxia cell lines treated with various concentrations of AuNC, revealing no discernible impact on cell viability after 24 and 48 h of incubation. However, it is noteworthy that the cell viability percentage decreases in both the A549 normoxia and hypoxia cell lines as the concentration of BBR increases. This reduction in cell viability can be attributed to BBR's well-known anticancer properties. Berberine directly targets the nucleic acids and certain proteins within the cell, leading to cell cycle arrest and the activation of apoptosis signalling pathways.[61,62]

Table 1 ROS generation efficiency percentage for the following samples under NIR irradiation (808 nm, 0.75 W cm^{-2}) for 30 min

Sample	ROS generation efficiency (%)
BBR	16
AuNC	25
AuNC@BBR	25
AuNC@BBR@Ghost	80

3.7 The intracellular ROS generation in A549 cells by AuNC@BBR@Ghost associated PDT

To evaluate the potential of AuNC@BBR@Ghost in PDT for cancer cell treatment, we utilized DCFDA staining to measure intracellular ROS levels before and after irradiation in both normoxia and hypoxia cells, as shown in Fig. 7. ROS production is the primary driver of cytotoxicity in cancer cells when exposed to light or laser irradiation in the presence of a PDT agent.[64] Therefore, we utilized DCFDA staining to quantify ROS generation induced by AuNC@BBR@Ghost following PDT treatment in both normoxia and hypoxia cells.

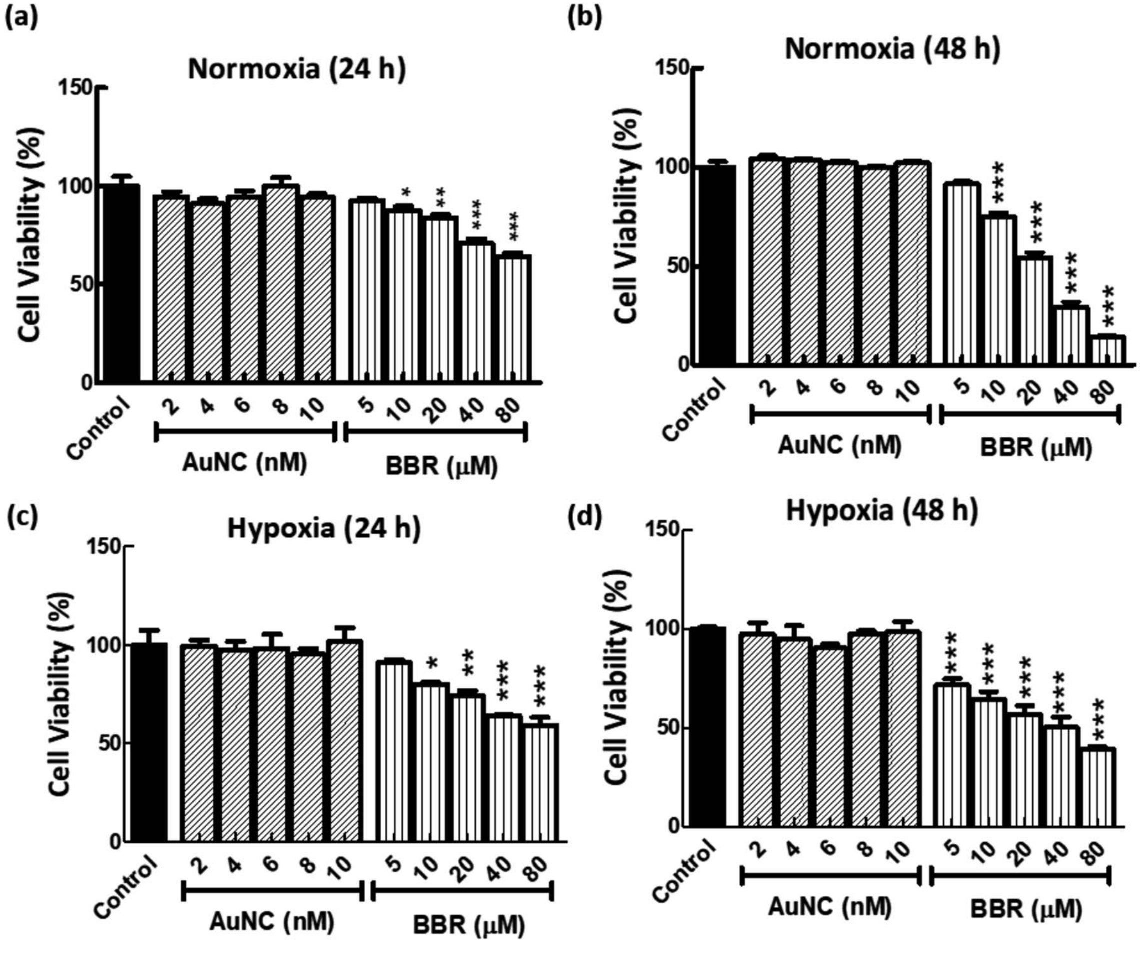

Fig. 6 Cell viability study using MTT assay for A549 cells treated with various concentration of AuNC and BBR for incubation periods of 24 h and 48 h. (a and b) cells under normoxic conditions and (c and d) cells under hypoxic conditions ($n = 3$). $*p < 0.05$, $**p < 0.01$, $***p < 0.001$. Data are mean ± SD.

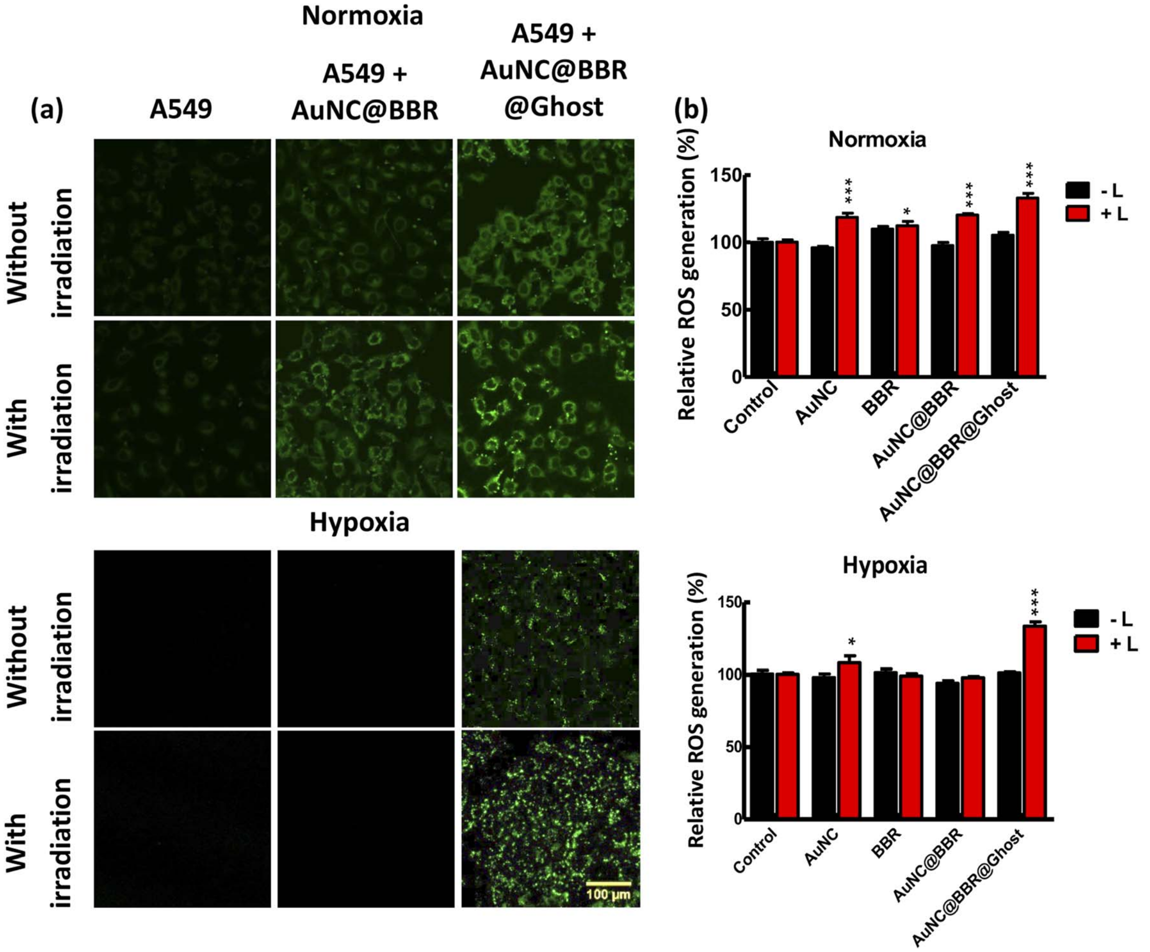

Fig. 7 Detection of intracellular ROS generation in A549 cell line under both normoxia and hypoxia conditions. The detection was performed using an oxidized DCFDA probe incorporated into samples with and without NIR irradiation (wavelength: 808 nm; power density: 0.75 w cm^{-2}). (a) Fluorescence microscopic images (ex/em: 488/520–550 nm; objective: 20×) scale bar represents 100 μm; and (b) measurement of DCF fluorescence intensity ($n = 3$). *$p < 0.05$, **$p < 0.01$, ***$p < 0.001$ indicate significant difference between untreated and treated samples. Data are mean ± SD.

In Fig. 7(a), we observe the fluorescence signal of DCF. Control cells and cells subjected solely to laser treatment displayed no DCF fluorescence signal. Similarly, cells treated with AuNC@BBR in the absence of laser irradiation showed no DCF fluorescence. However, cells treated with AuNC@BBR-associated PDT exhibited ROS generation in normoxia cells. In contrast, hypoxia cells, deprived of oxygen, did not show a ROS signal in the AuNC@BBR-associated PDT sample. Intriguingly, when AuNC@BBR@Ghost was introduced into hypoxia cells, DCF fluorescence signals were observed in both normoxia and hypoxia cells. The corresponding fluorescence intensity of DCF in normoxia and hypoxia cells was quantified using a microplate reader, as presented in Fig. 7(b). Importantly, the fluorescent intensity data aligned well with the observations made in the confocal fluorescence images. It's also worth noting that AuNC can generate ROS when exposed to NIR irradiation, while BBR did not generate ROS when exposed to NIR light, as demonstrated in Fig. 3a and S5.† This correlation further supports the findings presented in the study.

3.8 Effects of the phototoxicity of AuNC@BBR@Ghost on A549 cells

To assess the phototoxicity of AuNC@BBR@Ghost in the context of PDT for cancer cell treatment, we employed a live/dead staining kit and MTT assay to distinguish between living and deceased cells before and after irradiation in both normoxia and hypoxia cells, as depicted in Fig. 8.

A live/dead assay utilizing violet fluorescent and DiOC5(3) was conducted to validate the therapeutic benefits of AuNC@BBR@Ghost photodynamic therapy in both normoxia and hypoxia cells, as illustrated in Fig. 8a. Strikingly, control cells and cells exposed exclusively to laser treatment did not exhibit any violet fluorescence signal. Similarly, cells treated with AuNC@BBR without laser irradiation did not display violet fluorescence. However, cells subjected to AuNC@BBR-associated PDT exhibited a limited violet fluorescence signal in the AuNC@BBR-associated PDT sample. Conversely, a substantial number of deceased cells were observed in the AuNC@BBR@Ghost group when exposed to NIR laser

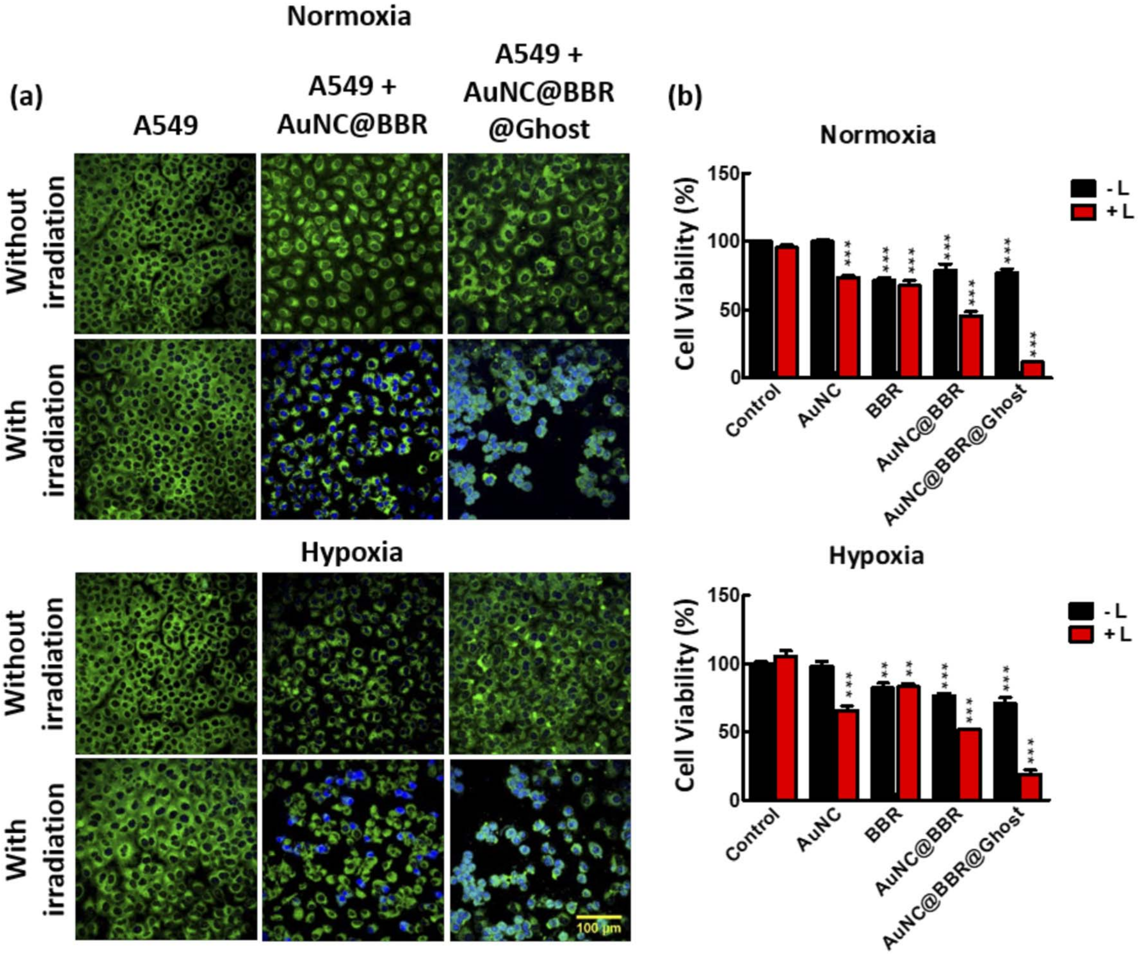

Fig. 8 Comparison of the PDT efficacy of AuNC@BBR with and without ghost treatment under NIR irradiation (wavelength: 808 nm; power density: 0.75 w cm^{-2}); (a) discrimination of live and dead A549 normoxia and hypoxia cell line using violet fluorescent and DiOC5(3) staining, observed through confocal fluorescence microscopy (objective: 20×). The scale bar represents 100 μm; (b) cell viability of A549 cells assessed through MTT assay. Cells were treated with AuNC, BBR, AuNC@BBR, and AuNC@BBR@Ghost associated PDT treatment ($n = 3$). *$p < 0.05$, **$p < 0.01$, ***$p < 0.001$ indicate significant difference between untreated and treated samples. Data are mean ± SD.

compared to the AuNC@BBR@Ghost without NIR irradiation. This finding indicates the effective therapeutic potential of AuNC@BBR@Ghost against cancer cells.

The phototherapeutic effectiveness of AuNC@BBR@Ghost against A549 cells under normoxia and hypoxia conditions was evaluated through the MTT assay, as depicted in Fig. 8b. The A549 cell line without any particle integration served as the control and displayed high cellular viability. Similarly, the cell line treated only with laser, without any particle application, showed high cellular viability. In Fig. 8(b), there is a noticeable reduction in cell viability percentage for cells subjected to AuNC@BBR@Ghost-associated PDT, compared to those treated with bare AuNCs, BBR-associated PDT, and the AuNC@BBR complex-associated PDT.

Based on these results, we propose that the AuNC@BBR@Ghost composite holds significant promise as a potential PDT agent. Further research, involving the delivery of AuNC@BBR@Ghost into a mice model, is crucial to gain a deeper understanding of how ghost cells enhance PDT efficiency in hypoxic tumor environments and to advance biomedical applications.

4. Conclusions

In this study, we synthesized and characterized a novel biomimetic nanocomposite, AuNC@BBR@Ghost, which incorporates AuNC@BBR complex into ghost cells. The synthesized AuNC demonstrated remarkable capability in generating ROS under NIR irradiation. This feature is crucial for its application in PDT, a promising approach for cancer treatment. AuNC@BBR@Ghost exhibited the ability to generate ROS even in hypoxic conditions, which are commonly found in the tumor microenvironment. This attribute is particularly valuable as it addresses a significant challenge in cancer therapy. Our results clearly demonstrate that AuNC@BBR@Ghost-associated PDT is highly effective in reducing the viability of A549 cancer cells, both in normoxic and hypoxic conditions. This effectiveness surpasses that of treatments with bare AuNC, BBR, or AuNC@BBR individually, indicating a collectively enhanced therapeutic effect. Furthermore, the preservation of the ghost cell structure and its oxygen-carrying capacity suggests that AuNC@BBR@Ghost can serve as an efficient drug delivery system. In conclusion, AuNC@BBR@Ghost is a promising nanocomposite with the potential for selective and effective cancer therapy. Its ability to generate ROS in both normoxia and hypoxia, coupled with its biocompatibility and structural integrity, establishes it as a valuable candidate for further exploration in preclinical and clinical studies for cancer treatment. Additionally, the potential for targeted drug delivery through erythrocyte ghost cells opens avenues for personalized and precision medicine in cancer therapy.

Author contributions

WGP is responsible for data curation, formal analysis, and writing of the manuscript draft. RS, NSh, SCH, HHC, ESP, DB, VVT provided resources on the experiments, AVK and EVP helped on the method and data analysis, CLC is responsible for funding acquisition, supervision, project administration, data analysis, manuscript writing, review and editing.

Conflicts of interest

The authors declare there are no conflicts of interest to declare.

Acknowledgements

The authors would like to acknowledge the financial support by National Science and Technology Council (NSTC) of Taiwan (NSTC-109-2112-M-259-005-MY3). Work of ESP, NSh and VVT was supported by the Ministry of Science and Higher Education of the Russian Federation within the framework of state assignment (Project No. FSRR-2023-0007).

References

1 M. S. Muthu, D. T. Leong, L. Mei and S. S. Feng, *Theranostics*, 2014, **4**, 660–677.
2 L. Zhang and E. Wang, *Nano Today*, 2014, **9**, 132–157.
3 Y. Vlamidis and V. Voliani, *Front. Bioeng. Biotechnol.*, 2018, **6**, 143.
4 J. Zheng, P. R. Nicovich and R. M. Dickson, *Annu. Rev. Phys. Chem.*, 2007, **58**, 409–431.
5 P. Londoño-Larrea, J. P. Vanegas, D. Cuaran-Acosta, E. Zaballos-García and J. Pérez-Prieto, *Chem.—Eur. J.*, 2017, **23**, 8137–8141.
6 K. Huang, H. Ma, J. Liu, S. Huo, A. Kumar, T. Wei, X. Zhang, S. Jin, Y. Gan, P. C. Wang, S. He, X. Zhang and X.-J. Liang, *ACS Nano*, 2012, **6**, 4483–4493.
7 L. Y. Chen, C. W. Wang, Z. Yuan and H. T. Chang, *Anal. Chem.*, 2015, **87**, 216–229.
8 Z. Luo, K. Zheng and J. Xie, *Chem. Commun.*, 2014, **50**, 5143–5155.
9 L. Hu, L. Deng, S. Alsaiari, D. Zhang and N. M. Khashab, *Anal. Chem.*, 2014, **86**, 4989–4994.
10 J. Xie, Y. Zheng and J. Y. Ying, *J. Am. Chem. Soc.*, 2009, **131**, 888–889.
11 H. Qian, M. Zhu, Z. Wu and R. Jin, *Acc. Chem. Res.*, 2012, **45**, 1470–1479.
12 D. M. Chevrier, A. Chatt and P. Zhang, *J. Nanophotonics*, 2012, **6**, 064504.
13 C. A. J. Lin, T. Y. Yang, C. H. Lee, M. Zanella, J. K. Li, J. L. Shen, W. H. Chang, S. H. Huang, R. A. Sperling, H. H. Wang, H. I. Yeh and W. J. Parak, *ACS Nano*, 2009, **3**, 395–401.
14 R. Jin, C. Zeng, M. Zhou and Y. Chen, *Chem. Rev.*, 2016, **116**, 10346–10413.
15 X. Zhou, W. Xu, G. Liu, D. Panda and P. Chen, *J. Am. Chem. Soc.*, 2010, **132**, 138–146.
16 N. Kaur, R. N. Aditya, A. Singh and T. R. Kuo, *Nanoscale Res. Lett.*, 2018, **13**, 302.
17 E. S. Shibu, S. Sugino, K. Ono, H. Saito, A. Nishioka, S. Yamamura, M. Sawada, Y. Nosaka and V. Biju, *Angew Chem. Int. Ed. Engl.*, 2013, **52**, 10559–10563.
18 H. Kawasaki, S. Kumar, G. Li, C. Zeng, D. R. Kauffman, J. Yoshimoto, Y. Iwasaki and R. Jin, *Chem. Mater.*, 2014, **26**, 2777–2788.
19 D. Crawford, I. Zbinden, R. Moret and P. Cerutti, *Cancer Res.*, 1988, **48**, 2132–2134.
20 M. R. Detty, S. L. Gibson and S. J. Wagner, *J. Med. Chem.*, 2004, **47**, 3897–3915.
21 S. Cui, D. Yin, Y. Chen, Y. Di, H. Chen, Y. Ma, S. Achilefu and Y. Gu, *ACS Nano*, 2013, **7**, 676–688.
22 J. D. Bhawalkar, N. D. Kumar, C. F. Zhao and P. N. Prasad, *J. Clin. Laser Med. Surg.*, 1997, **15**, 201–204.
23 D. Jaque, L. Martinez Maestro, B. del Rosal, P. Haro-Gonzalez, A. Benayas, J. L. Plaza, E. Martin Rodriguez and J. Garcia Sole, *Nanoscale*, 2014, **6**, 9494–9530.
24 A. V. Kroll, R. H. Fang and L. Zhang, *Bioconjugate Chem.*, 2017, **28**, 23–32.
25 I. T. Kostic, V. L. Ilic, V. B. Dordevic, K. M. Bukara, S. B. Mojsilovic, V. A. Nedovic, D. S. Bugarski, D. N. Veljovic, D. M. Misic and B. M. Bugarski, *Colloids Surf., B*, 2014, **122**, 250–259.
26 M. Xuan, J. Shao and J. Li, *Natl. Sci. Rev.*, 2019, **6**, 551–561.
27 K. Bukara, S. Jovanic, I. T. Drvenica, A. Stancic, V. Ilic, M. D. Rabasovic, D. Pantelic, B. Jelenkovic, B. Bugarski and A. J. Krmpot, *J. Biomed. Opt.*, 2017, **22**, 26003.
28 C. Guido, G. Maiorano, C. Gutiérrez-Millán, B. Cortese, A. Trapani, S. D'Amone, G. Gigli and I. E. Palamà, *Appl. Sci.*, 2021, **11**, 2173.
29 L. Koleva, E. Bovt, F. Ataullakhanov and E. Sinauridze, *Pharmaceutics*, 2020, **12**, 276.
30 C. H. Villa, D. B. Cines, D. L. Siegel and V. Muzykantov, *Transfus. Med. Rev.*, 2017, **31**, 26–35.
31 D. G. Duff, A. Baiker and P. P. Edwards, *J. Chem. Soc. Chem. Commun.*, 1993, **9**, 2301–2309.
32 A. Kumar, Ekavali, K. Chopra, M. Mukherjee, R. Pottabathini and D. K. Dhull, *Eur. J. Pharmacol.*, 2015, **761**, 288–297.
33 S. K. Battu, M. A. Repka, S. Maddineni, A. G. Chittiboyina, M. A. Avery and S. Majumdar, *AAPS PharmSciTech*, 2010, **11**, 1466–1475.

34 S. Suganthi, R. Sivaraj and I. Enoch, *Nucleosides, Nucleotides Nucleic Acids*, 2019, **38**, 858–873.

35 B. J. R. Philogène, J. T. Arnason, G. H. N. Towers, Z. Abramowski, F. Campos, D. Champagne and D. M. Lachlan, *J. Chem. Ecol.*, 1984, **10**, 115–123.

36 Y. W. An, H. T. Jin, B. Yuan, J. C. Wang, C. Wang and H. Q. Liu, *Oncol. Lett.*, 2021, **21**, 359.

37 J. J. Inbaraj, B. M. Kukielczak, P. Bilski, S. L. Sandvik and C. F. Chignell, *Chem. Res. Toxicol.*, 2001, **14**, 1529–1534.

38 T. Z. Lopes, F. R. de Moraes, A. C. Tedesco, R. K. Arni, P. Rahal and M. F. Calmon, *Biomed. Pharmacother.*, 2020, **123**, 109794.

39 W. G. Pearl, E. V. Perevedentseva, A. V. Karmenyan, V. A. Khanadeev, S. Y. Wu, Y. R. Ma, N. G. Khlebtsov and C. L. Cheng, *J. Biophotonics*, 2021, e202100264, DOI: **10.1002/jbio.202100264**.

40 M. Li, H. Fang, Q. Liu, Y. Gai, L. Yuan, S. Wang, H. Li, Y. Hou, M. Gao and X. Lan, *Biomater. Sci.*, 2020, **8**, 1802–1814.

41 V. Gomez Flores, A. Martinez-Martinez, J. A. Roacho Perez, J. Acosta Bezada, F. S. Aguirre-Tostado and P. E. Garcia Casillas, *Materials*, 2021, **14**, 6390.

42 M. P. Patel, V. Siu, A. Silva-Garcia, Q. Xu, Z. Li and D. Oksenberg, *Drug Des., Dev. Ther.*, 2018, **12**, 1599–1607.

43 D. Gabrielli, E. Belisle, D. Severino, A. J. Kowaltowski and M. S. Baptista, *Photochem. Photobiol.*, 2007, **79**, 227–232.

44 W. Wang, W. Zhang, H. Sun, Q. Du, J. Bai, X. Ge and C. Li, *Dyes Pigm.*, 2019, **160**, 663–670.

45 N. A. Daghastanli, R. Itri and M. S. Baptista, *Photochem. Photobiol.*, 2008, **84**, 1238–1243.

46 C. Liu, H. Dong, N. Wu, Y. Cao and X. Zhang, *ACS Appl. Mater. Interfaces*, 2018, **10**, 6991–7002.

47 M. S. Diaz, M. L. Freile and M. I. Gutierrez, *Photochem. Photobiol. Sci.*, 2009, **8**, 970–974.

48 J. Heo, D. P. Murale, H. Y. Yoon, V. Arun, S. Choi, E. Kim, J. S. Lee and S. Kim, *Aggregate*, 2022, **3**, e159–e194.

49 Y. Gu, Z. Zhao, H. Su, P. Zhang, J. Liu, G. Niu, S. Li, Z. Wang, R. T. K. Kwok, X. L. Ni, J. Sun, A. Qin, J. W. Y. Lam and B. Z. Tang, *Chem. Sci.*, 2018, **9**, 6497–6502.

50 F. He, L. Zhu, X. Zhou, P. Zhang, J. Cheng, Y. Qiao, Y. Feng, S. Yue, M. Xu, J. Guan, X. Li, Z. Ao, M. Qin, Y. Hou and D. Han, *ACS Appl. Mater. Interfaces*, 2022, **14**, 26372–26381.

51 H. P. Fernandes, C. L. Cesar and L. Barjas-Castro Mde, *Rev. Bras. Hematol. Hemoter*, 2011, **33**, 297–301.

52 E. H. Eylar, M. A. Madoff, O. V. Brody and J. L. Oncley, *J. Biol. Chem.*, 1962, **237**, 1992–2000.

53 F. Tokumasu, G. R. Ostera, C. Amaratunga and R. M. Fairhurst, *Exp. Parasitol.*, 2012, **131**, 245–251.

54 B. L. Horecker, *J. Biol. Chem.*, 1943, **148**, 173–183.

55 Y. C. Lin, L. W. Tsai, E. Perevedentseva, H. H. Chang, C. H. Lin, D. S. Sun, A. E. Lugovtsov, A. Priezzhev, J. Mona and C. L. Cheng, *J. Biomed. Opt.*, 2012, **17**, 101512.

56 F. Meng and A. I. Alayash, *Anal. Biochem.*, 2017, **521**, 11–19.

57 X. Shi, W. Yang, Q. Ma, Y. Lu, Y. Xu, K. Bian, F. Liu, C. Shi, H. Wang, Y. Shi and B. Zhang, *Theranostics*, 2020, **10**, 11607–11621.

58 E. Perevedentseva, Y. C. Lin, A. Karmenyan, K. T. Wu, A. Lugovtsov, E. Shirshin, A. Priezzhev and C. L. Cheng, *Materials*, 2021, **14**, 5920.

59 J. Zheng, C. Zhang and R. M. Dickson, *Phys. Rev. Lett.*, 2004, **93**, 077402.

60 A. K. Sahoo, S. Banerjee, S. S. Ghosh and A. Chattopadhyay, *ACS Appl. Mater. Interfaces*, 2014, **6**, 712–724.

61 L. M. Ortiz, P. Lombardi, M. Tillhon and A. I. Scovassi, *Molecules*, 2014, **19**, 12349–12367.

62 M. Tillhon, L. M. Guaman Ortiz, P. Lombardi and A. I. Scovassi, *Biochem. Pharmacol.*, 2012, **84**, 1260–1267.

63 H. H. Deng, K. Y. Huang, C. T. Zhu, J. F. Shen, X. P. Zhang, H. P. Peng, X. H. Xia and W. Chen, *J. Phys. Chem. Lett.*, 2021, **12**, 876–883.

64 A. El-Hussein and M. R. Hamblin, *IET Nanobiotechnol.*, 2017, **11**, 173–178.